



1 **Estimation of surface ammonia concentrations and emissions in**  
2 **China from the polar-orbiting Infrared Atmospheric Sounding**  
3 **Interferometer and the FY-4A Geostationary Interferometric**  
4 **Infrared Sounder**

5 Pu Liu<sup>1</sup>, Jia Ding<sup>1</sup>, Lei Liu<sup>1</sup>, Wen Xu<sup>2</sup>, Xuejun Liu<sup>2</sup>

6 <sup>1</sup> School of Earth and Environmental Sciences, Lanzhou University, Lanzhou, 730000, China

7 <sup>2</sup> College of Resources and Environmental Sciences, Centre for Resources, Environment and Food Security, Key Lab of Plant-  
8 Soil Interactions of MOE, China Agricultural University, Beijing 100193, China

9 Correspondence to: Lei Liu ([liuleigeo@lzu.edu.cn](mailto:liuleigeo@lzu.edu.cn))

10

11 **Abstract**

12 Ammonia (NH<sub>3</sub>) is the most important alkaline gas in the atmosphere, which has negative effects on  
13 biodiversity, ecosystems, soil acidification and human health. China has largest NH<sub>3</sub> emissions in the  
14 world mainly associated with agricultural sources including nitrogen fertilizer and livestock. However,  
15 there is still a limited number of ground monitoring sites in China, hindering our understanding of both  
16 surface NH<sub>3</sub> concentrations and emissions. In this study, using the polar-orbiting satellite (IASI) and  
17 Fengyun-4 geostationary satellite (GIIRS), we analyzed the changes of hourly NH<sub>3</sub> concentrations, and  
18 estimated surface NH<sub>3</sub> concentrations and NH<sub>3</sub> emissions in China. GIIRS-derived NH<sub>3</sub> concentration in  
19 daytime was generally higher than that at night, with high values during 8:00-18:00. Satellite-derived  
20 surface NH<sub>3</sub> concentration was generally consistent with the ground observation data with R-square at



21 0.72-0.81 and slope equal to 1.03. Satellite-based  $\text{NH}_3$  emissions ranged from 12.99-17.77 Tg N  $\text{yr}^{-1}$   
22 during 2008-2019. Spatially, high values of  $\text{NH}_3$  emissions mainly occurred in the North China Plain,  
23 Northeast China and Sichuan Basin, while low values were mainly distributed in western China (Qinghai-  
24 Tibet Plateau). Our study shows a high predictive power of using satellite data to estimate surface  $\text{NH}_3$   
25 concentration and  $\text{NH}_3$  emissions over multiple temporal and spatial scales, which provide an important  
26 reference for understanding  $\text{NH}_3$  changes over China.

## 27 **1 Introduction**

28 Ammonia ( $\text{NH}_3$ ) is a highly active gas in the atmosphere and the most important alkaline gas, playing an  
29 important role in atmospheric chemistry (Fowler et al., 2013).  $\text{NH}_3$  reacts with acid pollutants ( $\text{SO}_2$  and  
30  $\text{NO}_x$ ) to form fine particulate matters (such as  $\text{PM}_{2.5}$ ), leading to haze pollution. In addition, the  
31 deposition of  $\text{NH}_3$  and  $\text{NH}_4^+$  could also cause environmental problems such as water eutrophication,  
32 biodiversity loss and soil acidification (Paerl et al., 2014). To provide a scientific basis of dealing with  
33  $\text{NH}_3$  pollution, it is urgent to accurately estimate both surface  $\text{NH}_3$  concentrations and emissions in China.

34  
35 Surface  $\text{NH}_3$  concentration can be estimated by ground measurements and model simulations. Ground  
36 measurements are considered to be the most accurate quantitative method. Current national  $\text{NH}_3$   
37 observation networks in China include the National Nitrogen Deposition Monitoring Network (NNDMN)  
38 established by China Agricultural University (Xu et al., 2015) and the Ammonia Monitoring Network  
39 (AMoN-China) established based on the Chinese Ecosystem Research Network (CERN) (Pan et al., 2018).  
40 The NNDMN can measure ground  $\text{NH}_3$  concentrations since 2010, while the AMoN-China only made



41 the measurements in 2015-2016. The above two monitoring networks both monitor surface NH<sub>3</sub>  
42 concentration on a monthly basis, and lack monitoring of the hourly NH<sub>3</sub> changes. Some studies have  
43 carried out research on the intra-day/hourly changes of NH<sub>3</sub> concentrations based on ground observations.  
44 Werner et al. (2017) measured hourly NH<sub>3</sub> concentration in 2012 at the Harwell site in the United  
45 Kingdom, and found that high NH<sub>3</sub> concentration usually occurred in the afternoon. Similarly, Kutzner  
46 et al. (2021) observed the hourly NH<sub>3</sub> concentration on the SIRTAs Observatory in Paris and found NH<sub>3</sub>  
47 concentration is highest in the late afternoon. Pandolfi et al. (2012) studied the day-night cycle of NH<sub>3</sub>  
48 concentration at the two stations in Barcelona in summer, and found that the NH<sub>3</sub> concentration was  
49 highly associated with local meteorology and traffic emissions. However, there are still a limited number  
50 of monitoring sites on the hourly NH<sub>3</sub> changes in China.

51  
52 Agricultural fertilizer and livestock production have led to a large amount of NH<sub>3</sub> emissions. China's  
53 cultivated land area accounts for only 8% of the world, but it consumes about 30% of the world's nitrogen  
54 (N) fertilizer. Estimation of NH<sub>3</sub> emissions is mainly based on a bottom-up method, using NH<sub>3</sub> source  
55 statistics (fertilization, animal husbandry, etc.) and emission factors. Zhou et al. calculated the annual  
56 farmland NH<sub>3</sub> emission ( $3.96 \pm 0.76$  Tg N yr<sup>-1</sup>) in China based on the bottom-up method, which is 40%  
57 higher than the emission in IPCC tier 1 guidelines (Zhou et al., 2016). Zhang et al. reassessed China's  
58 NH<sub>3</sub> emissions based on the mass balance method, and found NH<sub>3</sub> emissions increased from  $12.1 \pm 0.8$  in  
59 2000 to  $15.6 \pm 0.9$  Tg N yr<sup>-1</sup> in 2015, with an annual growth rate of 1.9% (Liu et al., 2017). Fu et al.  
60 estimated that China's NH<sub>3</sub> emissions increased from 4.7 in 1980 to 11 Tg N yr<sup>-1</sup> in 2016. Although many  
61 studies regarding NH<sub>3</sub> emission have been carried out in China, great uncertainties and large ranges (7-



62 16 Tg N yr<sup>-1</sup>) still existed in the estimates of China's NH<sub>3</sub> emissions (Dong et al., 2010; Huang et al.,  
63 2012; Kang et al., 2016).

64

65 Besides the bottom-up estimates, some studies used data assimilation methods by ground monitoring data  
66 to constrain NH<sub>3</sub> emission estimates. Paulot et al. (2014) assimilated the GEOS-Chem with ground  
67 observations of wet N<sub>r</sub> deposition, and estimated China's NH<sub>3</sub> emission as 8.4 Tg N yr<sup>-1</sup> in 2008 with  
68 seasonal NH<sub>3</sub> emission peaked in summer. Gilliland et al. (2003) used the data assimilation method by  
69 the air quality model (CMAQ) with the wet NH<sub>4</sub><sup>+</sup> concentration data from the USA National Atmospheric  
70 Deposition Program Network, and found that obvious seasonal differences appeared in NH<sub>3</sub> emissions  
71 linked to N fertilizer and temperature. Kong et al. (2019) carried out inversion through assimilating  
72 surface AMoN NH<sub>3</sub> observation data, and improved the accuracy of temporal and spatial pattern of NH<sub>3</sub>  
73 emission in China.

74

75 In recent years, atmospheric remote sensing has developed rapidly, which can monitor NH<sub>3</sub> at a global  
76 scale including the polar-orbiting satellite instruments such as the Tropospheric emission spectrometer  
77 (TES), Infrared Atmospheric Sounding Interferometer (IASI), Cross-track Infrared Sounder (CrIS),  
78 Atmospheric Infrared Sounder (AIRS), and Greenhouse Gases Observing Satellite (GOSAT) (Someya et  
79 al., 2020). There have been many studies reporting the effectiveness of using satellite data to study NH<sub>3</sub>  
80 dynamics. Pinder et al. (2011) found that TES observation can capture spatial-temporal NH<sub>3</sub> patterns  
81 compared with surface measurement; Van Damme et al. (2014b) studied the seasonal and annual NH<sub>3</sub>  
82 changes in the northern and southern hemisphere using the IASI NH<sub>3</sub> column data, and found that the



83 seasonality in the southern hemisphere is mainly related to biomass burning; Shephard and Cady-Pereira  
84 (2015) developed the CrIS NH<sub>3</sub> inversion algorithms, and found that CrIS can capture the global spatial  
85 distribution of NH<sub>3</sub> concentration; Warner et al. (2016) identified the main hotspots of agricultural NH<sub>3</sub>  
86 regions using AIRS, such as South Asia, China, the United States and some parts of Europe, and found  
87 that NH<sub>3</sub> concentrations increased at these agricultural regions since 2003. Besides, some studies also  
88 used the satellite measurements to improve the estimates of NH<sub>3</sub> emissions. Zhang et al. (2017) developed  
89 a top-down inversion method by using TES NH<sub>3</sub> observation to quantify China's NH<sub>3</sub> emission, and  
90 obtained annual NH<sub>3</sub> emission as 11.7 Tg N yr<sup>-1</sup> in 2008. Marais et al. (2021) estimated NH<sub>3</sub> emissions  
91 in the UK based on IASI and CrIS and found the relative errors of IASI-derived NH<sub>3</sub> emissions were 11-  
92 36% and 9-27% respectively; Van Damme et al. (2018) used the high-resolution IASI NH<sub>3</sub> maps to  
93 identify, classify and quantify NH<sub>3</sub> emission hotspots in the world, which is helpful to understand the  
94 man-made point NH<sub>3</sub> sources; Dammers et al. (2019) identified global 249 NH<sub>3</sub> emission point sources  
95 based on CrIS, which is about 2.5 times higher than that reported in the HTAPv2 emissions.

96  
97 Besides the polar-orbiting satellite, China's Geostationary Interferometric Infrared Sounder (GIIRS)  
98 onboard the Chinese FY-4A satellite can measure hourly changes of atmospheric NH<sub>3</sub> almost all of Asia  
99 per day, which provide great potential to study the diel cycle of NH<sub>3</sub>. In this study, GIIRS was used to  
100 study the NH<sub>3</sub> diel cycle (hourly changes), which is essential for understanding the differences between  
101 different times in a day by the polar-orbiting satellites (such as IASI at 9:30 and CrIS at 13:30). Second,  
102 the surface NH<sub>3</sub> concentration in China is estimated based on both GIIRS and IASI, which was then  
103 compared with the NNDMN. Third, NH<sub>3</sub> emission in China are calculated based on satellite-derived



104 surface  $\text{NH}_3$  concentration and the feedback relationship between surface  $\text{NH}_3$  concentration and emission  
105 by a chemistry transport model (GEOS-Chem). Finally, the spatial-temporal characteristics of satellite-  
106 derived surface  $\text{NH}_3$  concentration and emission were analyzed, and the uncertainties were discussed.

## 107 **2 Data and methods**

### 108 **2.1 Satellite GIIRS $\text{NH}_3$**

109 The Geostationary Interferometric Infrared Sounder (GIIRS) onboard the Fengyun-4A geostationary  
110 satellite (FY-4A) launched by China in 2016 is the world's first hyperspectral atmospheric infrared  
111 sounder. The FY-4A GIIRS detected spectral range is  $700\text{-}2250\text{ cm}^{-1}$ , including 1648 spectral channels  
112 and 14 radiations imaging channels, covering visible light, short, medium and long wave infrared bands.  
113 The spatial resolution of the detector is 2.0 km in the visible band and 16 km in the infrared bands. It  
114 covers almost the whole of Asia and scans 10 times a day. The GIIRS can detect the temperature and  
115 humidity profiles and trace gases at high frequency.

116

117  $\text{NH}_3$  has two large absorption characteristics in the long wave infrared (about  $930\text{ cm}^{-1}$  and  $965\text{ cm}^{-1}$ ).  
118 The contribution of  $\text{NH}_3$  to the brightness temperature of these two bands is between 2-4 K. The core of  
119 inversion algorithms is based on the so-called hyperspectral radiation index (HRI), which quantifies the  
120 spectral characteristics of  $\text{NH}_3$ . The HRI index depends on whether the satellite instrument detects the  
121 presence of  $\text{NH}_3$ . The average value of HRI is 0 with the standard deviation as 1, and the HRI range is [-  
122 1,1]. The algorithms for estimating IASI  $\text{NH}_3$  column concentration is to convert HRI into a column using  
123 the so-called neural network (Clarisse et al., 2021).



124 In this study, we used hourly  $\text{NH}_3$  concentrations during 2019-2020 (from November in 2019 to October  
125 in 2020) to study  $\text{NH}_3$  diel cycle with a resolution of  $0.5^\circ$ . The original data is in H5 format, and the unit  
126 of  $\text{NH}_3$  is  $\text{molec.cm}^{-2}$ . The data is processed with MATLAB software. First, observations with  
127 considerable uncertainties (relative error exceeds 50%) and high clouds (cloud cover exceeds 20%) were  
128 removed. Secondly, the world standard time (UTC) by GIRS is converted to local time, and the data in  
129 H5 format is converted to TIFF data.

## 130 **2.2 Satellite IASI $\text{NH}_3$**

131 IASI instrument is on board the polar solar synchronous Metop-A platform. It has been running stably  
132 since 2006 to measure the infrared radiation emitted by the earth (Van Damme et al., 2014a). IASI can  
133 measure the infrared radiation emitted by the earth's surface and atmosphere in the spectral range of 645-  
134  $2760 \text{ cm}^{-1}$ . It can observe the world twice a day, and cross the equator at 9:30 and 21:30 local time, with  
135 a spatial resolution of 12 km at nadir. However, only daytime satellite measurements are used, because  
136 nighttime measurements usually have greater uncertainties related to thermal contrasts (Van Damme et  
137 al., 2017).

138

139 The cloud free reanalysis product of total  $\text{NH}_3$  column (v3R-ERA5) was used here. The properties of  
140 IASI  $\text{NH}_3$  data include  $\text{NH}_3$  column concentration, longitude, latitude, measurement time, cloud cover,  
141 uncertainty, solar zenith angle and other parameters. The daily  $\text{NH}_3$  column concentration from 2008 to  
142 2019 was used. The format of the original data is NC format, and the unit is  $\text{molec.cm}^{-2}$ . The observation  
143 data of with cloud cover larger than 20% and the uncertainty above 50% are removed. We gridded the  
144 data to  $0.1^\circ$  by using the arithmetic average methods.



### 145 **2.3 Ground NH<sub>3</sub> measurements**

146 Surface NH<sub>3</sub> concentrations in the NNDMN were used to compare with the satellite estimates including  
147 43 observation stations. The land types of the NNDMN sites cover cities, farmland, coastal areas, forests  
148 and grasslands. Measurements during the period from January 2010 to December 2015 by the NNDMN  
149 were used. Surface NH<sub>3</sub> concentrations were measured using an active DELTA (DEnuder for Long-Term  
150 Atmospheric sampling) (Flechard et al., 2011). For the hourly measurements, we collected the data from  
151 the published papers including 5 sites including Xianghe (39.75 °N, 116.96 °E, 2017.12 -2018.2) (He et  
152 al., 2020), Fudan University (31.30 °N, 121.50 °E, 2013.7.1-2014.9.30) (Wang et al., 2015), Dianhushan  
153 (31.09 °N, 120.98 °E, 2014.3.1-2014.6.30) (Wang et al., 2015), Jinshan Chemical Industry Park (30.73 °N,  
154 121.27 °E, 2014.1.6-2014.6.30) (Wang et al., 2015), and Gucheng (39.15 °N, 115.73 °E, 2016.3-2017.5)  
155 (Kuang et al., 2020). The Xianghe site in Hebei Province and Dianhushan site in Shanghai represent rural  
156 environments; Jinshan Chemical Industry Park represents industrial environments; Gucheng site in Hebei  
157 and the Fudan University site in Shanghai represent urban environments.

### 158 **2.4 GEOS-Chem**

159 The GEOS-Chem model version 12.3.0 is a three-dimensional chemistry transport model developed by  
160 Harvard University, which has been widely used in the field of atmospheric studies (Eastham et al., 2014).  
161 The nested regional model in Asia was used in this study driven by assimilated GEOS-5 meteorological  
162 data at a horizontal resolution of  $1/2^\circ \times 2/3^\circ$ . Dry deposition calculation in GEOS-Chem follows a  
163 standard resistance-in-series model (Wesely, 1989), while wet deposition includes both convective  
164 updraft and large-scale precipitation scavenging (Jacob, 1999). The GEOS-Chem model here does not  
165 consider land-atmosphere bi-directional NH<sub>3</sub> exchange and the NH<sub>3</sub> flux was parameterized as uncoupled



166 emission and dry deposition processes. Anthropogenic emissions over China were from the Regional  
167 Emission in Asia (REAS-v2) inventory. The GEOS-Chem outputs of NH<sub>3</sub> concentrations include 47  
168 layers from the ground to the top of atmosphere, which is used to capture NH<sub>3</sub> vertical profiles. The  
169 feedback between surface NH<sub>3</sub> concentration and emissions was also calculated by GEOS-Chem.

## 170 2.5 Satellite-based surface NH<sub>3</sub> estimates and emissions

171 Surface NH<sub>3</sub> concentrations were estimated using the satellite NH<sub>3</sub> columns as well as NH<sub>3</sub> vertical  
172 profiles. To gain the continuous vertical NH<sub>3</sub> profile, the Gaussian function was used to fit the 47 layers'  
173 NH<sub>3</sub> concentrations. A three parameter Gaussian function was used to fit NH<sub>3</sub> vertical profiles at each  
174 grid box from GEOS-Chem according to previous studies (Liu et al., 2019).

$$175 \rho(Z) = \sum_{i=1}^n \rho_{max,i} e^{-\left(\frac{Z-Z_{0,i}}{\sigma_i}\right)^2}, \quad (1)$$

176 where  $Z$  is the height of a layer in the ACTM;  $\rho_{max}$ ,  $Z_0$  and  $\sigma$  are the maximum of NH<sub>3</sub> concentration,  
177 the corresponding height with the maximum of NH<sub>3</sub> concentration and the thickness of NH<sub>3</sub> concentration  
178 layer (one standard error of Gaussian function).

179

180 The satellite-derived NH<sub>3</sub> concentration at the height of  $h_G$  can be calculated as:

$$181 S_{G\_NH_3} = S_{trop} \times \frac{\rho(h_G)}{\int_0^{h_{trop}} \rho(Z) dx} \times \frac{G_{ACTM}^{1-24}}{G_{ACTM}^{overpass}}, \quad (2)$$

182 where  $\frac{\rho(h_G)}{\int_0^{h_{trop}} \rho(Z) dx}$  represents the ratio of NH<sub>3</sub> concentration at the height of  $h_G$  to total columns

183  $(\int_0^{h_{trop}} \rho(Z) dx)$ ;  $S_{trop}$  represents satellite-derived NH<sub>3</sub> columns;  $\frac{G_{ACTM}^{1-24}}{G_{ACTM}^{overpass}}$  is the ratio of average surface

184 NH<sub>3</sub> concentration ( $G_{ACTM}^{1-24}$ ) to that at satellite overpass time ( $G_{ACTM}^{overpass}$ ) by an ACTM.



185 The mass balance method (Geddes and Martin, 2017; Cooper et al., 2017; Lamsal et al., 2011) was used  
186 to exploit the feedback ratio of surface  $\text{NH}_3$  concentrations and  $\text{NH}_3$  emissions (Marais et al., 2021):

$$187 \quad E_s = S_{G\_NH_3} \times \left( \frac{E}{G_{G\_NH_3}} \right)_m, \quad (3)$$

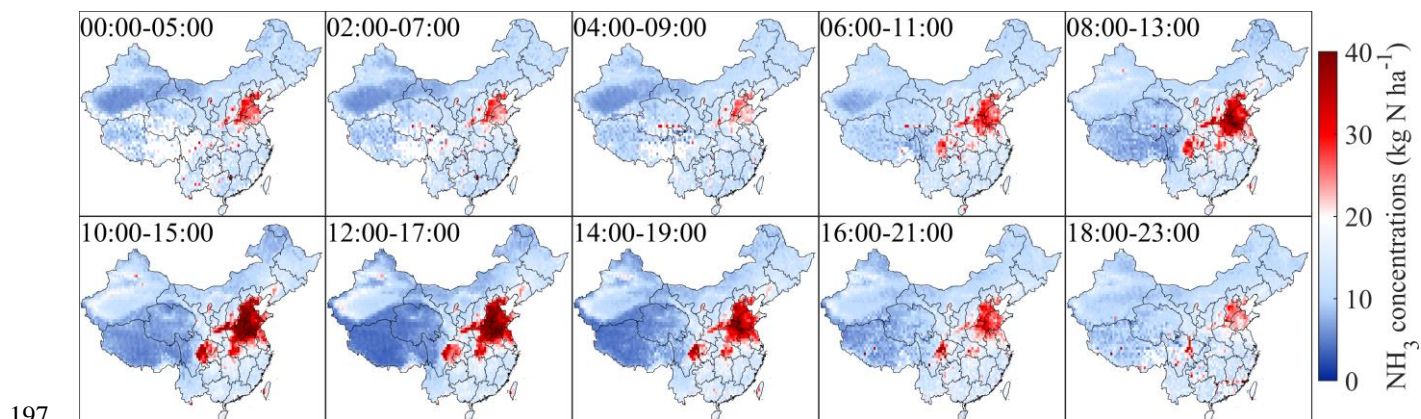
188 where  $E_s$  is satellite-based  $\text{NH}_3$  emissions;  $S_{G\_NH_3}$  is the satellite-derived surface  $\text{NH}_3$  concentrations;

189  $\left( \frac{E}{G_{G\_NH_3}} \right)_m$  is the ratio of surface  $\text{NH}_3$  concentrations and  $\text{NH}_3$  emissions simulated by the GEOS-Chem.

## 190 3 Results and discussions

### 191 3.1 GIRS-based hourly $\text{NH}_3$ concentrations during 2019-2020

192 Fig. 1 shows the hourly  $\text{NH}_3$  concentrations observed from GIRS during 2019-2020. Daytime  $\text{NH}_3$   
193 columns were significantly higher than those at night. The intra-day hourly  $\text{NH}_3$  columns showed an  
194 overall increase first, then a decrease, with high values during 8:00-18:00. The increase in temperature  
195 enhanced the volatilization of  $\text{NH}_3$ , which may explain high values of  $\text{NH}_3$  concentration during the  
196 daytime.



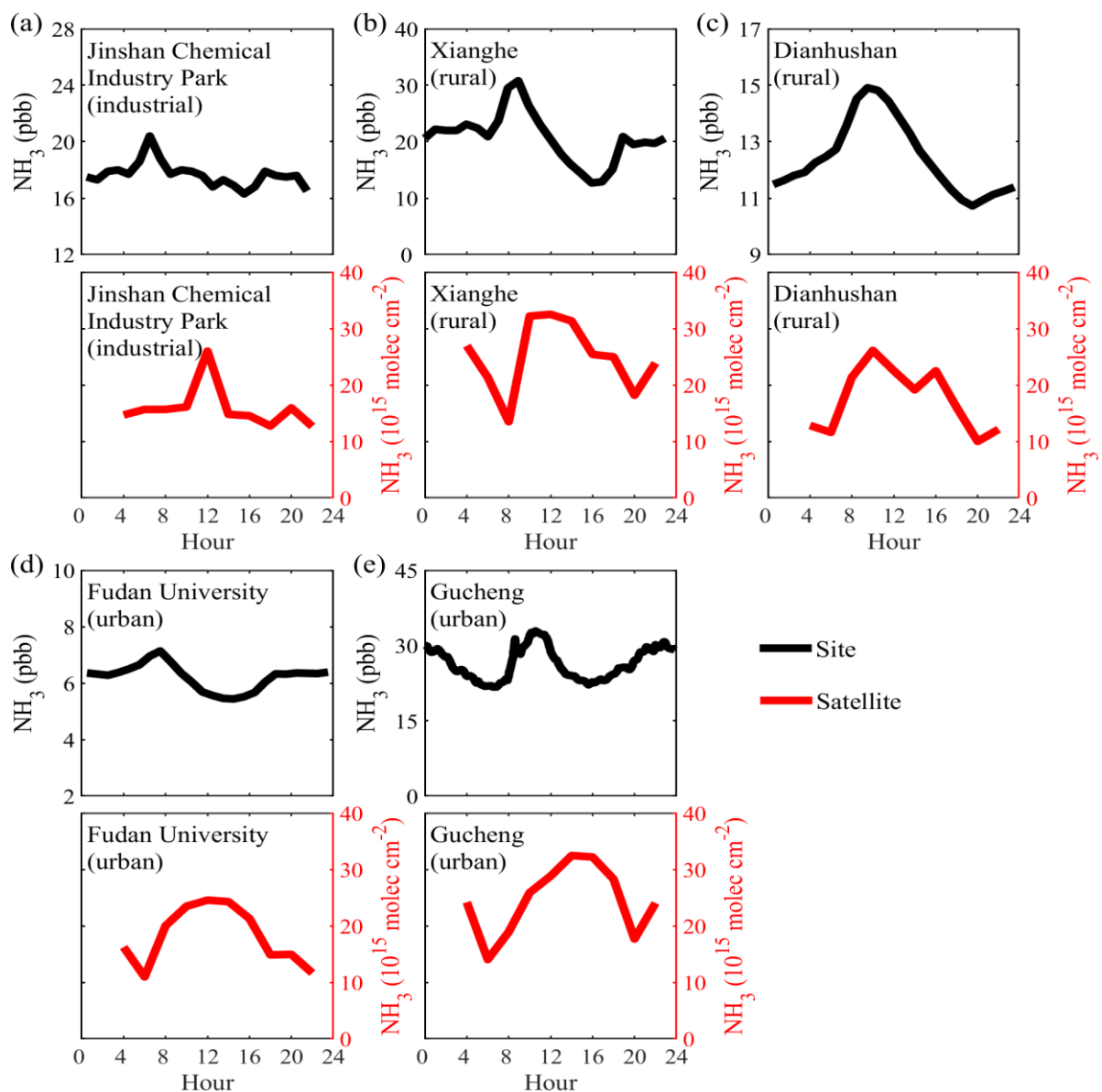
197  
198 **Figure 1.** Annual  $\text{NH}_3$  columns for each of the 10 GIRS overpass time periods during 2019-2020



199 Ground-based measurements of hourly  $\text{NH}_3$  concentration are very lacking, and the timespan may be  
200 different from GIIRS measurements. Here we only used them to show the hourly patterns of  $\text{NH}_3$   
201 concentration (Fig. 2). The Xianghe site in Hebei Province and Dianhushan site in Shanghai represent  
202 rural environments; Jinshan Chemical Industry Park represents industrial environments; Gucheng site in  
203 Hebei and the Fudan University site in Shanghai represent urban environments.

204

205  $\text{NH}_3$  concentration in the rural environment basically shows a normal distribution, and high  $\text{NH}_3$   
206 concentration generally appears between 8:00-18:00, which may be related to agricultural activities and  
207 temperature. In the industrial environment (Jinshan Chemical Industry Park, JSP),  $\text{NH}_3$  concentration  
208 fluctuates irregularly, and two peaks appear at 12:00 and 6:00-8:00, while for other time  $\text{NH}_3$   
209 concentration tends to be stable. In the urban environment, the changes of  $\text{NH}_3$  concentration by satellite  
210 at the Gucheng site are more consistent with ground monitoring, showing a clear peak around 9:00-13:00;  
211  $\text{NH}_3$  concentration at the Fudan University site gradually decreases from the morning peak to the  
212 afternoon. The evaporation of dew may drive the  $\text{NH}_3$  increase from the morning to the noon (Wang et  
213 al., 2015).  $\text{NH}_3$  concentration in cities (Gucheng and Fudan University) has double peaks between 6:00-  
214 8:00 and 18:00-19:00, which may be also related with traffic emissions. In summary, except the industrial  
215 sites, hourly  $\text{NH}_3$  in China have a large variability between day and night and the hourly  $\text{NH}_3$  patterns  
216 affected by many factors, of which anthropogenic emissions and temperature seem to be the most  
217 important driving factors.



218

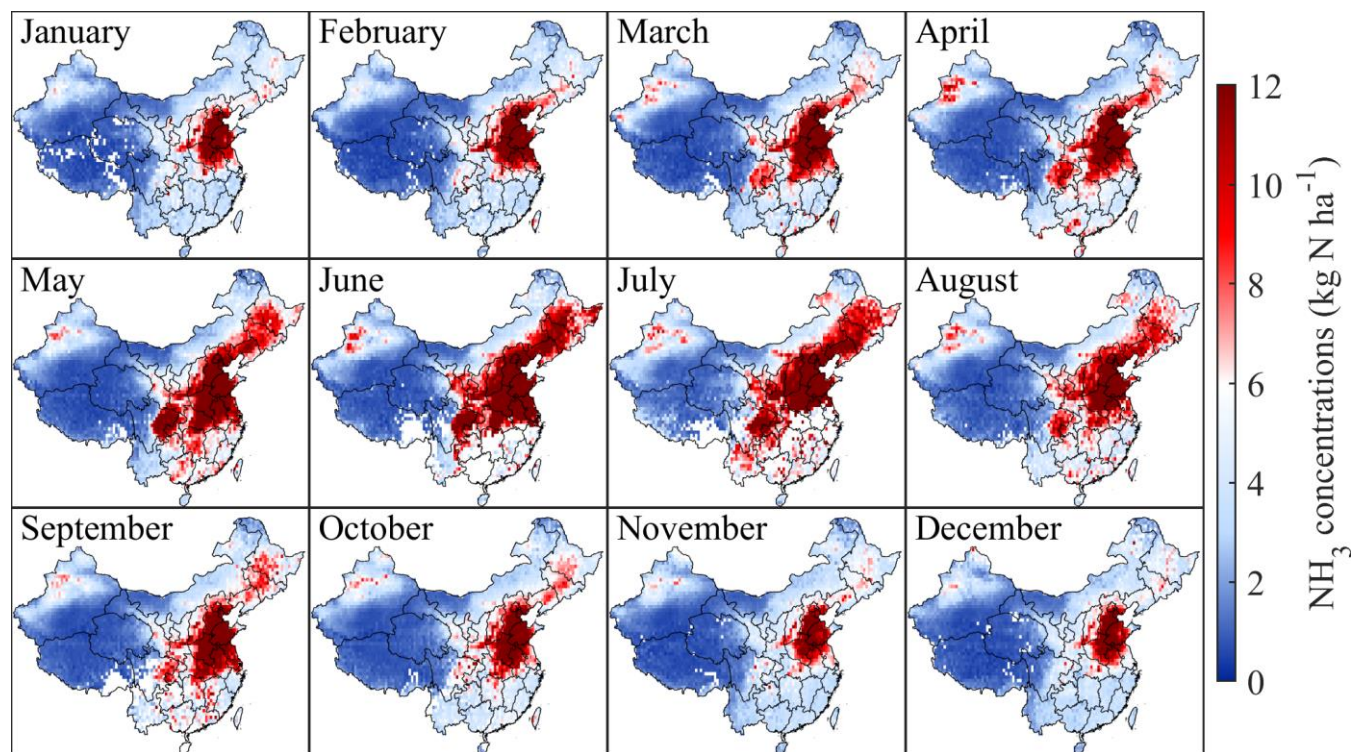
219 **Figure 2.** GIIRS-based and measured hourly  $\text{NH}_3$  concentrations at five sites including Jinshan Chemical  
220 Industry Park (JSP, a), Xianghe (XH, b), Dianhushan (DSL, c), Fudan University (FDU, d) and Gucheng  
221 (GC, e)

222



223 Spatial distribution of GIRS-based surface  $\text{NH}_3$  concentration across China had large variability. High  
224  $\text{NH}_3$  concentration is mainly concentrated in the North China Plain, with an average of  $12 \mu\text{g N m}^{-3}$ ,  
225 followed by Northeastern China, Xinjiang and the middle and lower reaches of the Yangtze River ( $4\text{--}8$   
226  $\mu\text{g N m}^{-3}$ ); low values ( $<2 \mu\text{g N m}^{-3}$ ) are mainly concentrated in the Qinghai-Tibet Plateau. High surface  
227  $\text{NH}_3$  concentration appeared in July ( $6.79 \mu\text{g N m}^{-3}$ ), and the lowest values appeared in November ( $3.26$   
228  $\mu\text{g N m}^{-3}$ ). There are obvious seasonal changes in surface  $\text{NH}_3$  concentration in the NCP with high values  
229 in summer, and low values in winter, related to both agricultural N fertilizer and higher temperature.

230



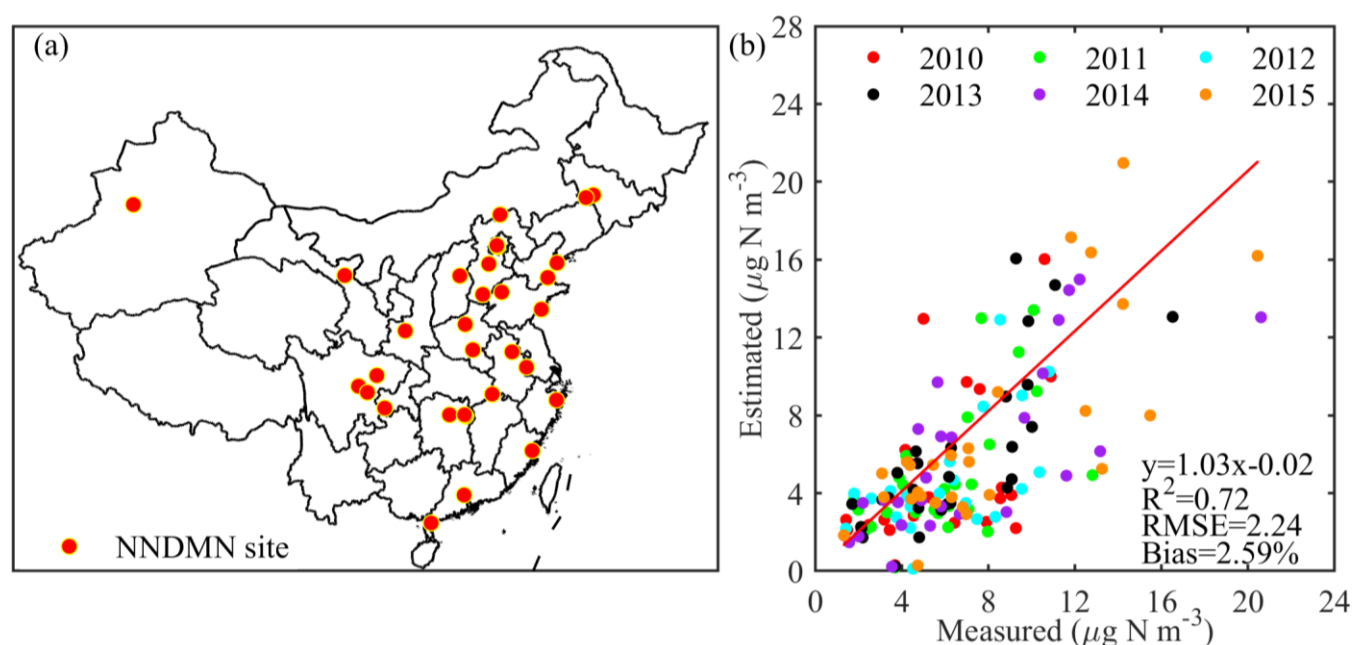
231

232 **Figure 3.** Spatial distribution of the monthly surface  $\text{NH}_3$  concentration in China by GIRS in 2019-2020



### 233 3.2 IASI-based NH<sub>3</sub> surface concentrations

234 The observation data of the NNDMN in China was collected to compare with IASI-derived surface NH<sub>3</sub>  
235 concentration. In general, a good consistency was found between measurements and satellite estimates  
236 with the regression R<sup>2</sup> as 0.72 and the RMSE as 2.24 μg N m<sup>-3</sup>. The coefficient of the fitted line is 1.03≈1  
237 and the bias is 2.59%.

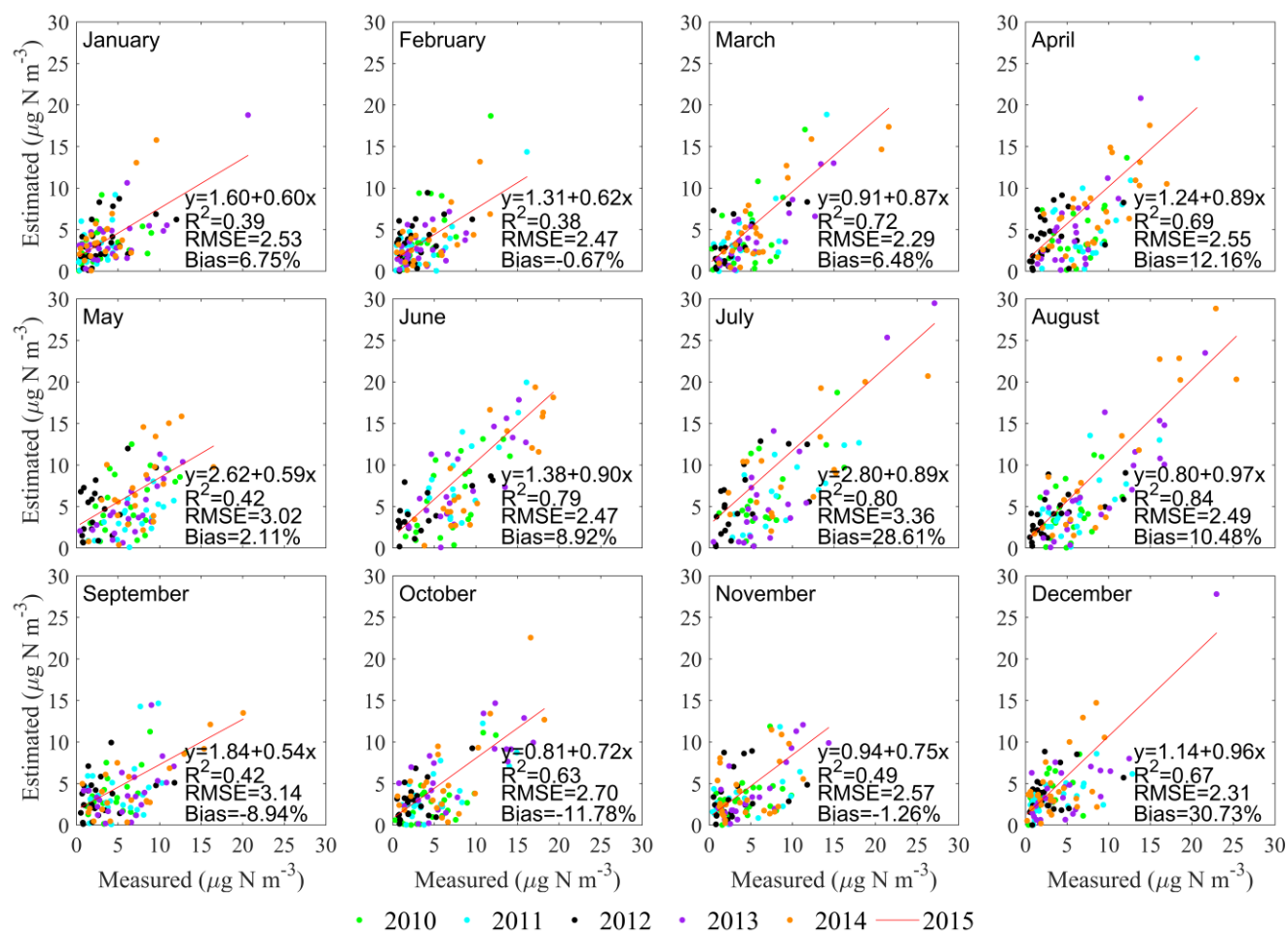


238  
239 **Figure 4.** Comparison of IASI surface NH<sub>3</sub> concentrations with NNDMN measurements. (a) the locations  
240 of NNDMN; (b) the regression results between satellite-estimates and measurements.

241  
242 Monthly regression R<sup>2</sup> between the satellite-derived NH<sub>3</sub> concentration and the measured NH<sub>3</sub> was 0.37-  
243 0.81. The regression R<sup>2</sup> reached the maximum value of 0.81 in July and August. The RMSE ranged from  
244 2.22- 3.54 μg N m<sup>-3</sup>, which reached the maximum value of 3.54 μg N m<sup>-3</sup> in July, and reached the smallest  
245 in March (2.22 μg N m<sup>-3</sup>). The bias is basically less than 30% for all months, and reached the minimum



246 value of 0.71% in February, indicating that the monthly IASI-derived surface concentration obtained are  
247 consistent with measurements.

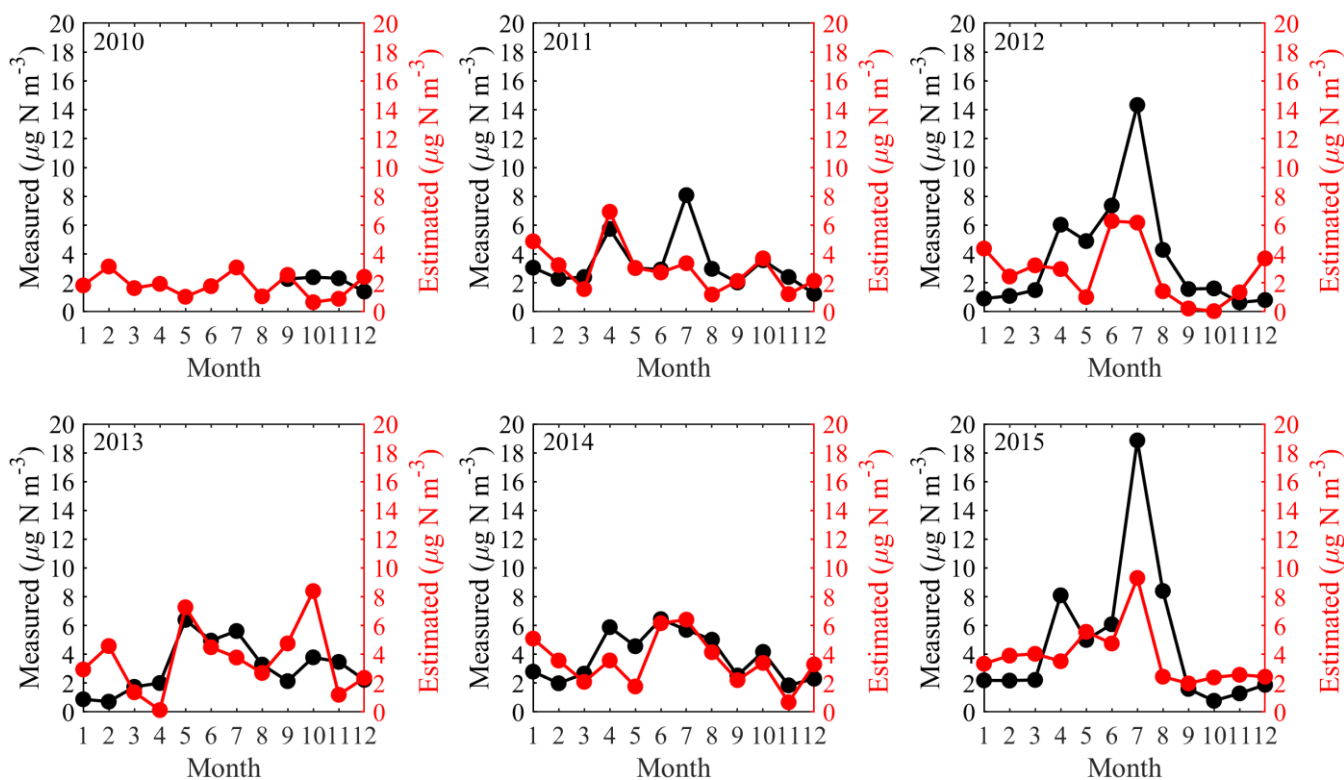


249 **Figure 5.** Comparison of monthly average values of IASI-derived and observed NH<sub>3</sub> surface  
250 concentrations in 2010-2015

251  
252 Fig. 6 shows the monthly changes of surface NH<sub>3</sub> concentrations in Huinong County in Ningxia from  
253 2010 to 2015 for a total of 72 months during 2010-2015. Surface NH<sub>3</sub> concentration retrieved by IASI  
254 was compared with the observation data at Huinong. The highest value of each year basically appeared



255 from June to August, and the lowest values appeared from December to January. In the past 6 years, the  
256 maximum measured  $\text{NH}_3$  concentrations appeared in July 2015 ( $18.9 \mu\text{g N m}^{-3}$ ), and the minimum  
257 appeared in November 2012 ( $0.6 \mu\text{g N m}^{-3}$ ). The observation data and satellite data have the same seasonal  
258 changes.

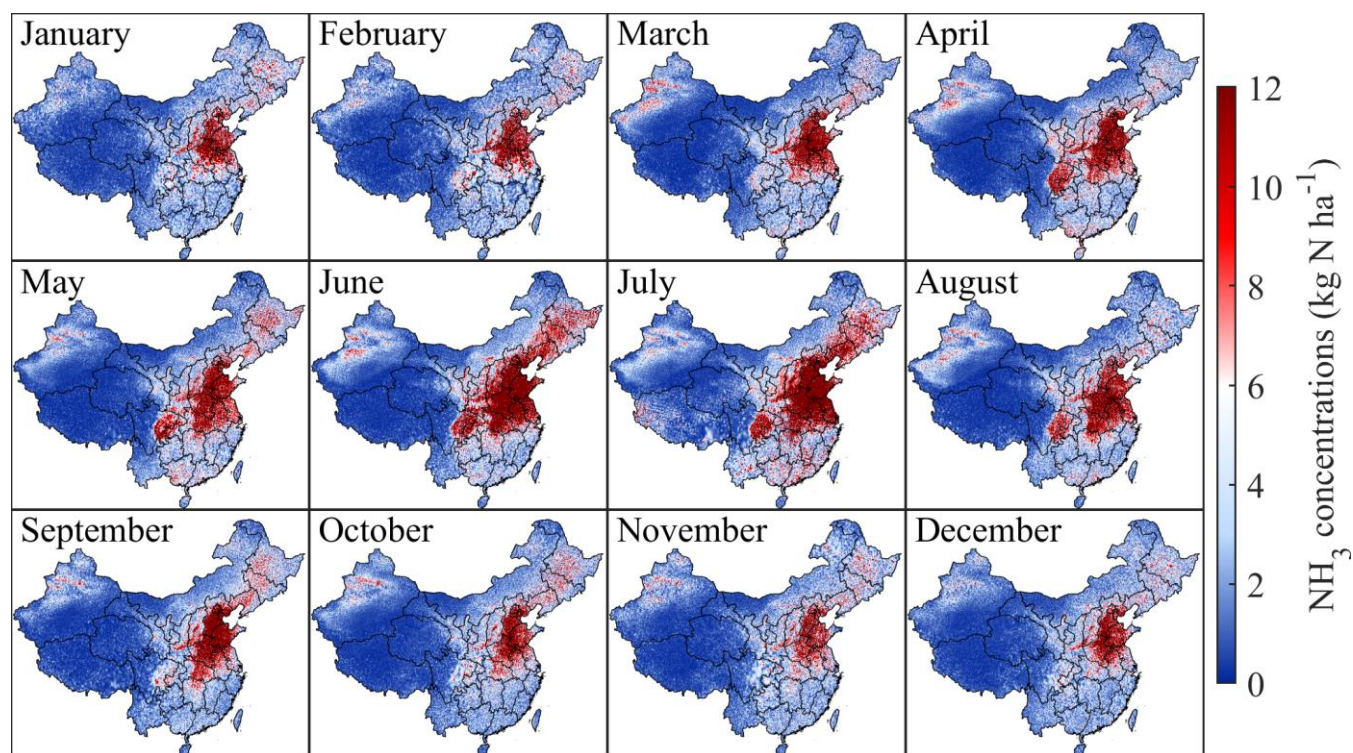


259  
260 **Figure 6.** Monthly changes of  $\text{NH}_3$  concentrations in Huinong County in Ningxia from 2010 to 2015 for  
261 a total of 72 months during 2010-2015.

262  
263 Fig. 3 and Fig. 7 show the spatial distribution of GIIRS-derived and IASI-derived surface  $\text{NH}_3$   
264 concentration in 2019. The spatial distribution and gradients of surface  $\text{NH}_3$  concentration by the GIIRS  
265 and IASI have the same gradients from eastern to western regions. One notable difference occurred in the



266 middle and lower reaches of the Yangtze River in June and July since the GIRS observations were  
267 affected by clouds and have missing data.



268  
269 **Figure 7.** Spatial distribution of the monthly surface  $\text{NH}_3$  concentration in China by IASI in 2019

270

### 271 3.3 IASI-derived $\text{NH}_3$ emissions

272 Based on the top-down estimates, China's  $\text{NH}_3$  emissions ranged from 12.99-17.77 Tg N  $\text{yr}^{-1}$  during  
273 2008-2019. From 2008 to 2015,  $\text{NH}_3$  emissions increased from 12.99 Tg N  $\text{yr}^{-1}$  to 17.06 Tg N  $\text{yr}^{-1}$ . Since  
274 2008, the temperature in China has risen steadily (Ding et al., 2007), which promotes the volatilization of  
275  $\text{NH}_3$ , which partly explains the increase in  $\text{NH}_3$  emissions from 2008 to 2015. After 2015,  $\text{NH}_3$  emissions  
276 fluctuated and changed slightly (16.08-17.77 Tg N  $\text{yr}^{-1}$ ). Compared with other studies, the change of  $\text{NH}_3$   
277 emissions from 2008 to 2015 is consistent with previous estimates, and the overall  $\text{NH}_3$  emissions show



278 an upward trend (Zhang et al., 2021; Fu et al., 2020; Zhang et al., 2018; Ma, 2020; Kang et al., 2016).  
279 Our estimates are on the rise as a whole, but the calculated values are generally lower than those by Fu et  
280 al. (around 15 Tg N yr<sup>-1</sup>), but larger than those by EDGAR and Kang et al. (2016).

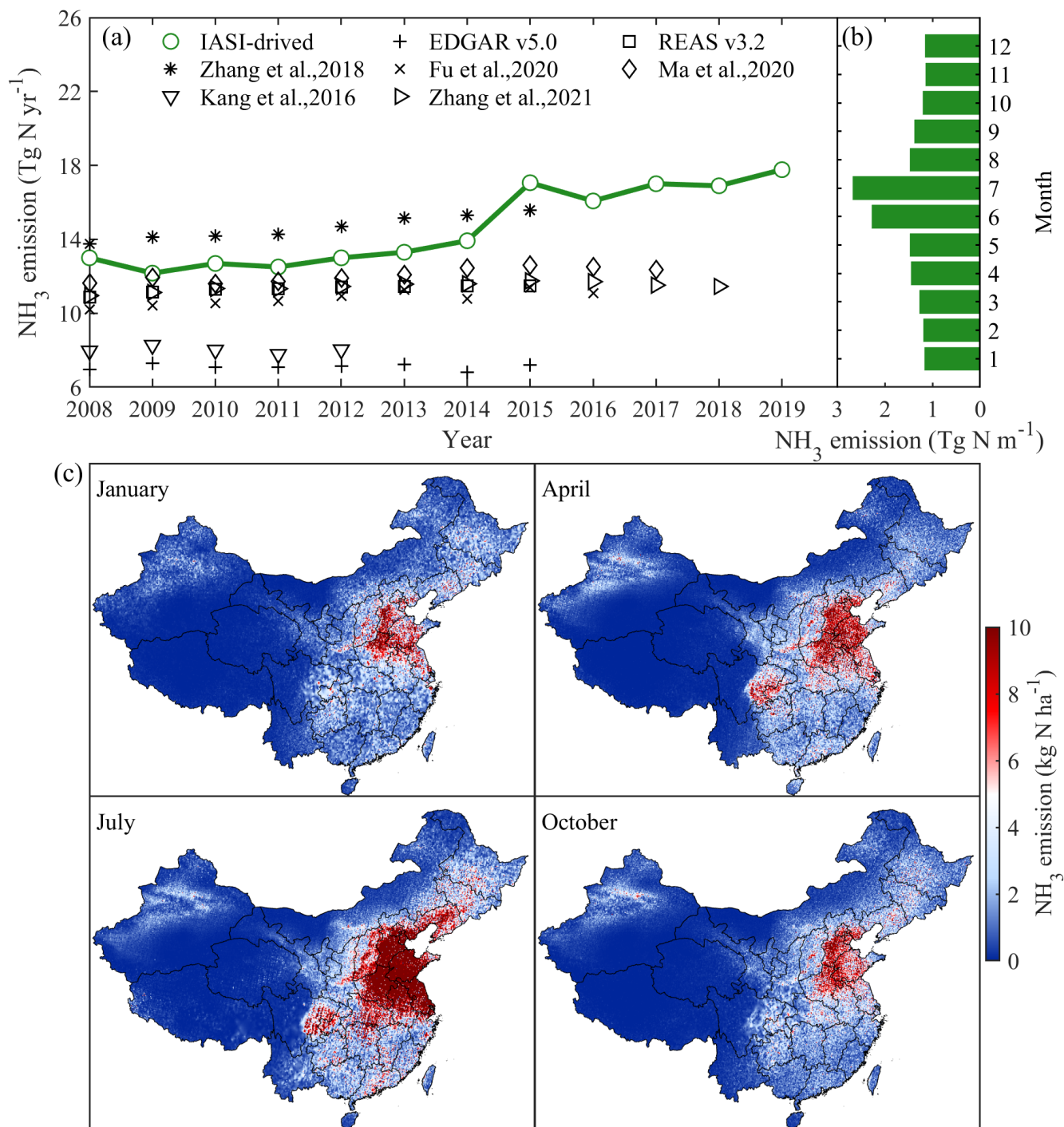
281

282 In terms of spatial distribution, high NH<sub>3</sub> emissions are generally distributed in the North China Plain,  
283 Sichuan Basin, Northeast China and Xinjiang, while the low values are mainly distributed in the  
284 Southwest China (especially Qinghai-Tibet Plateau). The North China Plain is China's granary, with  
285 developed agriculture and animal husbandry, high population densities and strong human activities  
286 (including vehicle emissions). In contrast, South China is rich in rainfall, which promotes the deposition  
287 of NH<sub>3</sub> and suppresses its volatilization to a certain extent.

288

289 The spatial distribution of NH<sub>3</sub> emissions in January, April, July and October were selected to characterize  
290 the seasonal variations. The average emissions for the four months were 1.15 kg N ha<sup>-1</sup>, 1.31 kg N ha<sup>-1</sup>,  
291 2.31 kg N ha<sup>-1</sup> and 1.16 kg N ha<sup>-1</sup> in January, April, July and October, indicating that NH<sub>3</sub> emission is the  
292 highest in summer and the lowest in winter. The annual average emission intensity of 2019 is 16.53 kg N  
293 ha<sup>-1</sup> (0.09-313.47 kg N ha<sup>-1</sup>). Fig. 8b shows the monthly changes in NH<sub>3</sub> emissions, which basically shows  
294 a normal distribution. High values are generally distributed in June and July, and low values are generally  
295 distributed in November and December. It reached the maximum monthly emission of 2.6 Tg N m<sup>-1</sup> in  
296 July 2019 and reached the minimum monthly emission in November and December (1.1 Tg N m<sup>-1</sup>).

297



298

299 **Figure 8.** Annual changes of NH<sub>3</sub> emissions (a), monthly changes of NH<sub>3</sub> emissions in 2019 (b) and  
 300 spatial distribution of NH<sub>3</sub> emissions by month in 2019 (c).



#### 301 **4 Limitations and outlook**

302 This study developed satellite-based surface  $\text{NH}_3$  concentration and emissions in China based on remote  
303 sensing data (IASI and GIIRS). However, several limitations have been identified in this study. First, the  
304 Fengyun geostationary satellite used in this study can achieve hourly  $\text{NH}_3$  concentrations, but the time  
305 series are still very short (2019-2020), and satellite observations are affected by clouds and meteorological  
306 conditions, resulting in missing values in parts of the Yangtze River Basin. Second, the spatial resolution  
307 of the  $\text{NH}_3$  vertical profile simulated by the atmospheric model is relatively coarse (0.5 degrees). In order  
308 to make it consistent with the spatial resolution of the remote sensing data, the outputs of GEOS-Chem  
309 (vertical profiles and feedback ratio between emissions and surface  $\text{NH}_3$  concentrations) were interpolated  
310 through resampling methods. Third, at present, there are more and more satellite sensors (GOSAT, CrIS,  
311 AIRS, etc.) that can monitor  $\text{NH}_3$  concentration. This study only used IASI and GIIRS, and in the future,  
312 data from different satellites can be merged to analyze  $\text{NH}_3$  changes on multiple temporal and spatial  
313 scales.

#### 314 **5 Conclusion**

315 We use GIIRS to study the  $\text{NH}_3$  diel cycle, and estimated surface  $\text{NH}_3$  concentrations and emissions based  
316 on IASI in China. There are obvious hourly changes in  $\text{NH}_3$  concentration in China using GIIRS. Overall,  
317  $\text{NH}_3$  concentration was larger at daytime than nighttime in China. Hourly  $\text{NH}_3$  concentrations at different  
318 land use show different patterns, but high values generally appear in 8:00-18:00. Comparing IASI-derived  
319 and observed  $\text{NH}_3$  surface concentrations by NNDMN from 2010 to 2015, the coefficient of the fitted  
320 line is  $1.03 \approx 1$ , and low bias is 3%, indicating satellite estimates have good consistency with the



321 measurements. IASI-derived China's  $\text{NH}_3$  emissions ranged from 12.99-17.77 Tg N yr<sup>-1</sup> during 2008-  
322 2019, among which  $\text{NH}_3$  emissions increased from 2008 to 2015. The emission intensity of  $\text{NH}_3$  in China  
323 presents a strong spatial heterogeneity, showing high in the eastern and low in the western. The high  
324 values are mainly distributed in the North China Plain and Sichuan Basin. High values are generally  
325 distributed in summer, and low values generally occurred in winter. This study provides an important  
326 reference basis for the formulation of  $\text{NH}_3$  pollution prevention and control policy in China.

### 327 **Data availability**

328 IASI data were obtained from the <https://iasi.aeris-data.fr/nh3/>. The GHIRS data were obtained from  
329 <https://zenodo.org/record/4540024>.

### 330 **Author contributions**

331 The study was conceived by LL, and data analysis were performed by JD. The paper was written by PL,  
332 with editing from WX and XL. LL was involved in obtaining the project grant and supervised the study.

### 333 **Competing interests**

334 The contact author has declared that neither they nor their co-authors have any competing interests.

### 335 **Acknowledgements**

336 This study is supported by the National Natural Science Foundation of China (42001347, 41705130, and  
337 41922037) and the Chinese State Key Research & Development Programme (2017YFC0210100,



338 2017YFD0200101). The analysis in this study is supported by the Supercomputing Center of Lanzhou  
339 University.

## 340 References

- 341 Clarisse, L., Van Damme, M., Hurtmans, D., Franco, B., Clerbaux, C., and Coheur, P. F.: The Diel Cycle of NH<sub>3</sub> Observed  
342 From the FY-4A Geostationary Interferometric Infrared Sounder (GIIRS), *Geophysical Research Letters*, 48,  
343 10.1029/2021gl093010, 2021.
- 344 Cooper, M., Martin, R. V., Padmanabhan, A., and Henze, D. K.: Comparing mass balance and adjoint methods for inverse  
345 modeling of nitrogen dioxide columns for global nitrogen oxide emissions, *J. Geophys. Res.-Atmos.*, 2017.
- 346 Dammers, E., McLinden, C. A., Griffin, D., Shephard, M. W., Van der Graaf, S., Lutsch, E., Schaap, M., Gainairu-Matz, Y.,  
347 Fioletov, V., Van Damme, M., Whitburn, S., Clarisse, L., Cady-Pereira, K., Clerbaux, C., Coheur, P. F., and Erisman, J. W.:  
348 NH<sub>3</sub> emissions from large point sources derived from CrIS and IASI satellite observations, *Atmos. Chem. Phys.*, 19, 12261-  
349 12293, 10.5194/acp-19-12261-2019, 2019.
- 350 Ding, Y. H., Ren, G. Y., Zhao, Z. C., Xu, Y., Luo, Y., Li, Q. P., and Zhang, J.: Detection, causes and projection of climate  
351 change over China: An overview of recent progress, *Adv. Atmos. Sci.*, 24, 954-971, 10.1007/s00376-007-0954-4, 2007.
- 352 Dong, W. X., Xing, J., and Wang, S. X.: Temporal and Spatial Distribution of Anthropogenic Ammonia Emissions in China:  
353 1994-2006, *Huanjing Kexue*, 31, 1457-1463, 2010.
- 354 Eastham, S. D., Weisenstein, D. K., and Barrett, S. R. H.: Development and evaluation of the unified tropospheric-stratospheric  
355 chemistry extension (UCX) for the global chemistry-transport model GEOS-Chem, *Atmospheric Environment*, 89, 52-63,  
356 10.1016/j.atmosenv.2014.02.001, 2014.
- 357 Flechard, C. R., Nemitz, E., Smith, R. I., Fowler, D., Vermeulen, A. T., Bleeker, A., Erisman, J. W., Simpson, D., Zhang, L.,  
358 Tang, Y. S., and Sutton, M. A.: Dry deposition of reactive nitrogen to European ecosystems: a comparison of inferential models  
359 across the NitroEurope network, *Atmos. Chem. Phys.*, 11, 2703-2728, 10.5194/acp-11-2703-2011, 2011.
- 360 Fowler, D., Coyle, M., Skiba, U., Sutton, M. A., Cape, J. N., Reis, S., Sheppard, L. J., Jenkins, A., Grizzetti, B., Galloway, J.  
361 N., Vitousek, P., Leach, A., Bouwman, A. F., Butterbach-Bahl, K., Dentener, F., Stevenson, D., Amann, M., and Voss, M.:  
362 The global nitrogen cycle in the twenty-first century, *Philos. Trans. R. Soc. B-Biol. Sci.*, 368, 13, 10.1098/rstb.2013.0164,  
363 2013.
- 364 Fu, H., Luo, Z. B., and Hu, S. Y.: A temporal -spatial analysis and future trends of ammonia emissions in China, *Sci. Total*  
365 *Environ.*, 731, 9, 10.1016/j.scitotenv.2020.138897, 2020.
- 366 Geddes, J. A. and Martin, R. V.: Global deposition of total reactive nitrogen oxides from 1996 to 2014 constrained with satellite  
367 observations of NO<sub>2</sub> columns, *Atmos. Chem. Phys.*, 17, 10071-10091, 2017.
- 368 Gilliland, A. B., Dennis, R. L., Roselle, S. J., and Pierce, T. E.: Seasonal NH<sub>3</sub> emission estimates for the eastern United States  
369 based on ammonium wet concentrations and an inverse modeling method, *J. Geophys. Res.-Atmos.*, 108, 12,  
370 10.1029/2002jd003063, 2003.
- 371 He, Y., Pan, Y. P., Zhang, G. Z., Ji, D. S., Tian, S. L., Xu, X. J., Zhang, R. J., and Wang, Y. S.: Tracking ammonia morning  
372 peak, sources and transport with 1 Hz measurements at a rural site in North China Plain, *Atmospheric Environment*, 235,  
373 117630, 10.1016/j.atmosenv.2020.117630, 2020.
- 374 Huang, X., Song, Y., Li, M. M., Li, J. F., Huo, Q., Cai, X. H., Zhu, T., Hu, M., and Zhang, H. S.: A high-resolution ammonia  
375 emission inventory in China, *Glob. Biogeochem. Cycle*, 26, 14, 10.1029/2011gb004161, 2012.
- 376 Jacob, D. J.: *Introduction to atmospheric chemistry*, Princeton University Press 1999.
- 377 Kang, Y. N., Liu, M. X., Song, Y., Huang, X., Yao, H., Cai, X., Zhang, H. S., Kang, L., Liu, X. J., Yan, X. Y., He, H., Zhang  
378 Q., Shao, M., and Zhu, T.: High-resolution ammonia emissions inventories in China from 1980 to 2012, *Atmospheric*  
379 *Chemistry and Physics*, 16, 2043-2058, 2016.
- 380 Kong, L., Tang, X., Zhu, J., Wang, Z. F., Pan, Y. P., Wu, H. J., Wu, L., Wu, Q. Z., He, Y. X., Tian, S. L., Xie, Y. Z., Liu, Z.  
381 R., Sui, W. X., Han, L. N. and Carmichael, G.: Improved inversion of monthly ammonia emissions in China based on the



- 382 Chinese ammonia monitoring network and ensemble Kalman filter, *Environmental science & technology*, 53, 12529-12538,  
383 2019.
- 384 Kuang, Y., Xu, W. Y., Lin, W. L., Meng, Z. Y., Zhao, H. R., Ren, S. X., Zhang, G., Liang, L. L., and Xu, X. B.: Explosive  
385 morning growth phenomena of  $\text{NH}_3$  on the North China Plain: Causes and potential impacts on aerosol formation, *Environ*  
386 *Pollut.*, 257, 113621, 10.1016/j.envpol.2019.113621, 2020.
- 387 Kutzner, R. D., Cuesta, J., Chelin, P., Petit, J.-E., Ray, M., Landsheere, X., Tournadre, B., Dupont, J.-C., Rosso, A., Hase, F.,  
388 Orphal, J., and Beekmann, M.: Diurnal evolution of total column and surface atmospheric ammonia in the megacity of Paris,  
389 France, during an intense springtime pollution episode, *Atmos. Chem. Phys.*, 21, 12091-12111, 10.5194/acp-21-12091-2021,  
390 2021.
- 391 Lamsal, L. N., Martin, R. V., Padmanabhan, A., Donkelaar, A. V., Zhang, Q., Sioris, C. E., Chance, K., Kurosu, T. P., and  
392 Newchurch, M. J.: Application of satellite observations for timely updates to global anthropogenic  $\text{NO}_x$  emission inventories,  
393 *Geophys. Res. Lett.*, 38, 185-193, 2011.
- 394 Liu, L., Zhang, X. Y., Xu, W., Liu, X. J., Li, Y., Lu, X. H., Zhang, Y. H., and Zhang, W. T.: Temporal characteristics of  
395 atmospheric ammonia and nitrogen dioxide over China based on emission data, satellite observations and atmospheric transport  
396 modeling since 1980, *Atmospheric Chemistry and Physics*, 17, 9365-9378, 10.5194/acp-17-9365-2017, 2017.
- 397 Liu, L., Zhang, X. Y., Wong, A. Y. H., Xu, W., Liu, X. J., Li, Y., Mi, H., Lu, X. H., Zhao, L. M., Wang, Z., Wu, X. D., and  
398 Wei, J.: Estimating global surface ammonia concentrations inferred from satellite retrievals, *Atmos. Chem. Phys.*, 19, 12051-  
399 12066, 10.5194/acp-19-12051-2019, 2019.
- 400 Ma, S. Y.: High-resolution assessment of ammonia emissions in China: Inventories, driving forces and mitigation,  
401 *Atmospheric Environment*, 229, 10, 10.1016/j.atmosenv.2020.117458, 2020.
- 402 Marais, E. A., Pandey, A. K., Van Damme, M., Clarisse, L., Coheur, P. F., Shephard, M. W., Cady-Pereira, K. E., Misselbrook,  
403 T., Zhu, L., Luo, G., and Yu, F. Q.: UK Ammonia Emissions Estimated With Satellite Observations and GEOS-Chem, *Journal*  
404 *of Geophysical Research: Atmospheres*, 126, e2021JD035237, 2021.
- 405 Paerl, H. W., Gardner, W. S., Mccarthy, M. J., Peierls, B. L., and Wilhelm, S. W.: Algal blooms: noteworthy nitrogen, *Science*,  
406 346, 175, 2014.
- 407 Pan, Y. P., Tian, S. L., Zhao, Y. H., Zhang, L., Zhu, X. Y., Gao, J., Huang, W., Zhou, Y. B., Song, Y., Zhang, Q., and Wang,  
408 Y. S.: Identifying Ammonia Hotspots in China Using a National Observation Network, *Environmental Science & Technology*,  
409 52, 3926-3934, 10.1021/acs.est.7b05235, 2018.
- 410 Pandolfi, M., Amato, F., Reche, C., Alastuey, A., Otjes, R. P., Blom, M. J., and Querol, X.: Summer ammonia measurements  
411 in a densely populated Mediterranean city, *Atmos. Chem. Phys.*, 12, 7557-7575, 10.5194/acp-12-7557-2012, 2012.
- 412 Paulot, F., Jacob, D. J., Pinder, R. W., Bash, J. O., Travis, K., and Henze, D. K.: Ammonia emissions in the United States,  
413 European Union, and China derived by high-resolution inversion of ammonium wet deposition data: Interpretation with a new  
414 agricultural emissions inventory (MASAGE\_NH3), *J. Geophys. Res.-Atmos.*, 119, 4343-4364, 10.1002/2013jd021130, 2014.
- 415 Pinder, R. W., Walker, J. T., Bash, J. O., Cady-Pereira, K. E., Henze, D. K., Luo, M. Z., Osterman, G. B., and Shephard, M.  
416 W.: Quantifying spatial and seasonal variability in atmospheric ammonia with in situ and space-based observations, *Geophys.*  
417 *Res. Lett.*, 38, 5, 10.1029/2010gl046146, 2011.
- 418 Shephard, M. W. and Cady-Pereira, K. E.: Cross-track Infrared Sounder (CrIS) satellite observations of tropospheric ammonia,  
419 *Atmos. Meas. Tech.*, 8, 1323-1336, 10.5194/amt-8-1323-2015, 2015.
- 420 Someya, Y., Imasu, R., Shiomi, K., and Saitoh, N.: Atmospheric ammonia retrieval from the TANSO-FTS/GOSAT thermal  
421 infrared sounder, *Atmospheric Measurement Techniques*, 13, 309-321, 2020.
- 422 Van Damme, M., Whitburn, S., Clarisse, L., Clerbaux, C., Hurtmans, D., and Coheur, P. F.: Version 2 of the IASI  $\text{NH}_3$  neural  
423 network retrieval algorithm: near-real-time and reanalysed datasets, *Atmos. Meas. Tech.*, 10, 4905-4914, 10.5194/amt-10-  
424 4905-2017, 2017.
- 425 Van Damme, M., Clarisse, L., Whitburn, S., Hadji-Lazaro, J., Hurtmans, D., Clerbaux, C., and Coheur, P. F.: Industrial and  
426 agricultural ammonia point sources exposed, *Nature*, 564, 99-103, 10.1038/s41586-018-0747-1, 2018.
- 427 Van Damme, M., Clarisse, L., Heald, C. L., Hurtmans, D., Ngadi, Y., Clerbaux, C., Dolman, A., Erisman, J. W., and Coheur,  
428 P.-F.: Global distributions, time series and error characterization of atmospheric ammonia ( $\text{NH}_3$ ) from IASI satellite  
429 observations, *Atmospheric chemistry and physics*, 14, 2905-2922, 2014a.



- 430 Van Damme, M., Clarisse, L., Heald, C. L., Hurtmans, D., Ngadi, Y., Clerbaux, C., Dolman, A. J., Erisman, J. W., and Coheur,  
431 P. F.: Global distributions, time series and error characterization of atmospheric ammonia ( $\text{NH}_3$ ) from IASI satellite  
432 observations, *Atmos. Chem. Phys.*, 14, 2905-2922, 10.5194/acp-14-2905-2014, 2014b.
- 433 Wang, S. S., Nan, J. L., Shi, C. Z., Fu, Q. Y., Gao, S., Wang, D. F., Cui, H. X., Saiz-Lopez, A., and Zhou, B.: Atmospheric  
434 ammonia and its impacts on regional air quality over the megacity of Shanghai, China, *Sci Rep*, 5, 15842, 10.1038/srep15842,  
435 2015.
- 436 Warner, J. X., Wei, Z. G., Strow, L. L., Dickerson, R. R., and Nowak, J. B.: The global tropospheric ammonia distribution as  
437 seen in the 13-year AIRS measurement record, *Atmos. Chem. Phys.*, 16, 5467-5479, 10.5194/acp-16-5467-2016, 2016.
- 438 Werner, M., Kryza, M., Geels, C., Ellermann, T., and Ambelas Skjøth, C.: Ammonia Concentrations Over Europe –  
439 Application of the WRF-Chem Model Supported with Dynamic Emission, *Polish Journal of Environmental Studies*, 26, 1323-  
440 1341, 10.15244/pjoes/67340, 2017.
- 441 Wesely, M. L.: Parameterization of surface resistances to gaseous dry deposition in regional-scale numerical models,  
442 *Atmospheric Environment*, 23, 1293-1304, 10.1016/0004-6981(89)90153-4, 1989.
- 443 Xu, W., Luo, X. S., Pan, Y. P., Zhang, L., Tang, A. H., Shen, J. L., Zhang, Y., Li, K. H., Wu, Q. H., Yang, D. W., Zhang, Y.  
444 Y., Xue, J., Li, W. Q., Li, Q. Q., Tang, L., Lu, S. H., Liang, T., Tong, Y. A., Liu, P., Zhang, Q., Xiong, Z. Q., Shi, X. J., Wu,  
445 L. H., Shi, W. Q., Tian, K., Zhong, X. H., Shi, K., Tang, Q. Y., Zhang, L. J., Huang, J. L., He, C. E., Kuang, F. H., Zhu, B.,  
446 Liu, H., Jin, X., Xin, Y. J., Shi, X. K., Du, E. Z., Dore, A. J., Tang, S., Collett, J. L., Goulding, K., Sun, Y. X., Ren, J., Zhang,  
447 F. S., and Liu, X. J.: Quantifying atmospheric nitrogen deposition through a nationwide monitoring network across China,  
448 *Atmos. Chem. Phys.*, 15, 12345-12360, 10.5194/acp-15-12345-2015, 2015.
- 449 Zhang, L., Chen, Y. F., Zhao, Y. H., Henze, D. K., Zhu, L. Y., Song, Y., Paulot, F., Liu, X. J., Pan, Y. P., Lin, Y., and Huang,  
450 B. X.: Agricultural ammonia emissions in China: reconciling bottom-up and top-down estimates, *Atmos. Chem. Phys.*, 18,  
451 339-355, 10.5194/acp-18-339-2018, 2018.
- 452 Zhang, X. M., Wu, Y. Y., Liu, X. J., Reis, S. F., Jin, J. X., Dragosits, U., Van Damme, M., Clarisse, L., Whitburn, S., Coheur,  
453 P.-F., and Gu B. J.: Ammonia emissions may be substantially underestimated in China, *Environmental science & technology*,  
454 51, 12089-12096, 10.1021/acs.est.7b02171, 2017.
- 455 Zhang, X. M., Ren, C. C., Gu, B. J., and Chen, D. L.: Uncertainty of nitrogen budget in China, *Environ. Pollut.*, 286, 9,  
456 10.1016/j.envpol.2021.117216, 2021.
- 457 Zhou, F., Ciais, P., Hayashi, K., Galloway, J., Kim, D. G., Yang, C. L., Li, S. Y., Liu, B., Shang, Z. Y., and Gao, S. S.: Re-  
458 estimating  $\text{NH}_3$  Emissions from Chinese Cropland by a New Nonlinear Model, *Environmental Science & Technology*, 50,  
459 564-572, 10.1021/acs.est.5b03156, 2016.
- 460